

# X-ray bursting neutron star atmosphere models using an exact relativistic kinetic equation for Compton scattering

V. Suleimanov<sup>1,2</sup>, J. Poutanen<sup>3</sup>, and K. Werner<sup>1</sup>

<sup>1</sup> Institut für Astronomie und Astrophysik, Kepler Center for Astro and Particle Physics, Universität Tübingen, Sand 1, 72076 Tübingen, Germany

e-mail: [suleimanov@astro.uni-tuebingen.de](mailto:suleimanov@astro.uni-tuebingen.de), [werner@astro.uni-tuebingen.de](mailto:werner@astro.uni-tuebingen.de)

<sup>2</sup> Kazan Federal University, Kremlevskaja str., 18, Kazan 420008, Russia

<sup>3</sup> Astronomy Division, Department of Physics, P.O. Box 3000, FI-90014 University of Oulu, Finland  
e-mail: [juri.poutanen@oulu.fi](mailto:juri.poutanen@oulu.fi)

Received 25 April 2012 / Accepted 13 July 2012

## ABSTRACT

**Context.** Theoretical spectra of X-ray bursting neutron star (NS) model atmospheres are widely used to determine the basic NS parameters such as their masses and radii. Compton scattering, which plays an important role in spectra formation at high luminosities, is often accounted for using the differential Kompaneets operator, while in other models a more general, integral operator for the Compton scattering kernel is used.

**Aims.** We construct accurate NS atmosphere models using for the first time an exact treatment of Compton scattering via the integral relativistic kinetic equation. We also test various approximations to the Compton scattering redistribution function and compare the results with the previous calculations based on the Kompaneets operator.

**Methods.** We solve the radiation transfer equation together with the hydrostatic equilibrium equation accounting exactly for the radiation pressure by electron scattering. We use the exact relativistic angle-dependent redistribution function as well as its simple approximate representations.

**Results.** We thus construct a new set of plane-parallel atmosphere models in local thermodynamic equilibrium (LTE) for hot NSs. The models were computed for six chemical compositions (pure H, pure He, solar H/He mix with various heavy elements abundances  $Z = 1, 0.3, 0.1,$  and  $0.01Z_{\odot}$ , and three surface gravities  $\log g = 14.0, 14.3,$  and  $14.6$ . For each chemical composition and surface gravity, we compute more than 26 model atmospheres with various luminosities relative to the Eddington luminosity  $L_{\text{Edd}}$  computed for the Thomson cross-section. The maximum relative luminosities  $L/L_{\text{Edd}}$  reach values of up to 1.1 for high gravity models. The emergent spectra of all models are redshifted and fitted by diluted blackbody spectra in the 3–20 keV energy range appropriate for the *RXTE/PCA*. We also compute the color correction factors  $f_c$ .

**Conclusions.** The radiative acceleration  $g_{\text{rad}}$  in our luminous, hot-atmosphere models is significantly smaller than in corresponding models based on the Kompaneets operator, because of the Klein-Nishina reduction of the electron scattering cross-section, and therefore formally “super-Eddington” model atmospheres do exist. The differences between the new and old model atmospheres are small for  $L/L_{\text{Edd}} < 0.8$ . For the same  $g_{\text{rad}}/g$ , the new  $f_c$  are slightly larger (by approximately 1%) than the old values. We also find that the model atmospheres, the emergent spectra, and the color correction factor computed using angle-averaged and approximate Compton scattering kernels differ from the exact solutions by less than 2%.

**Key words.** radiative transfer – scattering – methods: numerical – stars: atmospheres – stars: neutron – X-rays: stars

## 1. Introduction

X-ray bursting neutron stars (NSs) are members of low-mass X-ray binaries with quasi-periodical thermonuclear flashes on their surfaces (see reviews by Lewin et al. 1993; Strohmayer & Bildsten 2006). Thermonuclear burning occurs at the bottom of the freshly accreted matter and can be so powerful that the luminosity reaches the Eddington limit. These bursts lead to photospheric radius expansion (PRE) and are a potentially powerful tool for determining the NS masses and radii (Ebisuzaki 1987; Damen et al. 1990; van Paradijs et al. 1990). The knowledge of NS basic parameters is extremely important for establishing the physical properties (equation of state) of supra-nuclear dense matter in the NS inner cores (see Lattimer & Prakash 2007, for a review).

The precise radius determination of the NSs from X-ray bursts is impossible without accurate spectral models. The observed spectra of X-ray bursts are often well-fitted by a black-

body (Galloway et al. 2008). Theoretical models of hot NS atmospheres show (London et al. 1986; Lapidus et al. 1986; Pavlov et al. 1991) that the emergent spectra are close to diluted blackbody spectra  $F_E \approx f_c^{-4} B_E(f_c T_{\text{eff}})$  owing to strong energy exchange caused by Compton scattering. The color correction factor  $f_c \equiv T_c/T_{\text{eff}}$ , which relates the color temperature of the spectrum  $T_c$  to the effective temperature of the atmosphere  $T_{\text{eff}}$ , takes values of about 1.3–1.9. Theoretical dependences of the color correction factor on luminosity for various chemical compositions and gravities were computed by Suleimanov et al. (2011b, hereafter SPW11). The atmosphere models used in their work were based on the Kompaneets operator (Kompaneets 1957) description of Compton scattering. This approach was also used in most previous studies (London et al. 1986; Lapidus et al. 1986; Ebisuzaki 1987; Pavlov et al. 1991). The Kompaneets operator describes Compton scattering in the non-relativistic, isotropic, diffusion approximation, which should still be rather adequate for hot NS model atmospheres

with typical effective temperatures below  $\sim 2$  keV. On the other hand, Madej and collaborators (Madej 1991; Madej et al. 2004; Majczyna et al. 2005) used the integral description of Compton scattering employing the angle-averaged redistribution function (RF) derived by Guilbert (1981). A fully relativistic treatment of Compton scattering becomes important at luminosities close to the Eddington values, because of the reduction of the effective cross-section and the corresponding drop in the radiation pressure force. This obviously changes the maximum value of the luminosity where hydrostatic equilibrium can still be achieved, i.e. the actual value of the Eddington luminosity. This has important implications for the method of determining the NS masses and radii from PRE bursts, which is based on the Eddington luminosity (see Suleimanov et al. 2011a, hereafter S11). It is therefore, necessary to check the validity of model atmospheres and spectral properties computed with the Kompaneets operator by comparing the results with more accurate models based on an exact treatment of Compton scattering using relativistic kinetic equations.

Here we construct new models of hot NS atmospheres based on an exact treatment of Compton scattering that employs a fully relativistic, angle-dependent RF (Aharonian & Atoyan 1981; Prasad et al. 1986; Nagirner & Poutanen 1994; Poutanen & Svensson 1996). In Sect. 2, we present the main equations describing the atmosphere models as well as the methods for their solution. We also compare atmosphere models based on various RFs for Compton scattering and using the Kompaneets operator. In Sect. 3, we present a new set of atmosphere models, emergent spectra, and the color correction factors. We compare them to previous results obtained with the Kompaneets operator. In Sect. 4, we discuss applications of the new models to the observations of X-ray bursts and determination of the NS masses and radii. We summarize in Sect. 5. In Appendix A we derive the exact RF for Compton scattering. The details of the method of solution of the radiative transfer equation are presented in Appendix B. Comparison with the previous attempts to compute atmosphere models using integral approach to Compton scattering are given in Appendix C. And, finally, Appendix D presents the spectral characteristics of the models.

## 2. Method of atmosphere modeling

### 2.1. Main equations

A method for modeling hot X-ray bursting NS atmospheres that employs the Kompaneets operator for Compton scattering was described in detail in SPW11. Here we repeat the basic assumptions and emphasize the differences arising because of the new treatment of Compton scattering as well as radiation transfer.

We compute models in hydrostatic and radiative equilibrium in a plane-parallel approximation. The main input parameters are the chemical composition (particularly the hydrogen mass fraction  $X$ ), the surface gravity

$$g = \frac{GM}{R^2}(1+z), \quad (1)$$

and the relative NS luminosity  $l = L/L_{\text{Edd}}$ , where  $L_{\text{Edd}}$  is the Eddington luminosity measured at the NS surface

$$L_{\text{Edd}} = \frac{4\pi GMc}{\kappa_e}(1+z), \quad (2)$$

for the Thomson scattering opacity

$$\kappa_e = \sigma_T \frac{N_e}{\rho} \approx 0.2(1+X) \text{ cm}^2 \text{ g}^{-1}. \quad (3)$$

Here  $\sigma_T = 6.65 \times 10^{-25} \text{ cm}^2$  is the Thomson cross-section,  $\rho$  is the gas density, and  $N_e$  is the electron number density. The gravitational redshift is related to the NS parameters as

$$1+z = (1 - 2GM/c^2R)^{-1/2}. \quad (4)$$

We assume that the flux is constant throughout the NS surface. Our calculations are valid for a patch on the NS surface if instead of the relative luminosity we consider the relative flux,  $l = F/F_{\text{Edd}}^*$ , as a parameter, where

$$F_{\text{Edd}}^* = \frac{L_{\text{Edd}}}{4\pi R^2} = \frac{GMc}{R^2 \kappa_e}(1+z). \quad (5)$$

The effective temperature  $T_{\text{eff}}$  can be expressed via  $l$  as

$$T_{\text{eff}} = l^{1/4} T_{\text{Edd}}, \quad (6)$$

where the Eddington temperature  $T_{\text{Edd}}$  is the maximum possible effective temperature on the NS surface, which is evaluated using the Thomson scattering opacity

$$\sigma_{\text{SB}} T_{\text{Edd}}^4 = F_{\text{Edd}}^* = \frac{gC}{\kappa_e}. \quad (7)$$

The structure of the atmosphere for an X-ray bursting NS is described by a set of differential equations. The first one is the hydrostatic equilibrium equation

$$\frac{dP_g}{dm} = g - g_{\text{rad}}, \quad (8)$$

where  $g_{\text{rad}}$  is the radiative acceleration and  $P_g$  is the gas pressure and the column density  $m$  is defined as

$$dm = -\rho ds, \quad (9)$$

where  $s$  is the vertical distance.

The second equation is the radiation transfer equation for the specific intensity  $I(x, \mu)$  accounting for Compton scattering (see Appendix A for derivation). In the plane-parallel approximation, it has the form

$$\mu \frac{dI(x, \mu)}{d\tau(x, \mu)} = I(x, \mu) - S(x, \mu), \quad (10)$$

where

$$d\tau(x, \mu) = [\sigma(x, \mu) + k(x)] dm, \quad (11)$$

$\mu = \cos \theta$  is the cosine of the angle between the surface normal and the direction of radiation propagation,  $x = hv/m_e c^2$  is the photon energy in units of electron rest mass, and  $k(x)$  is the “true” absorption opacity. The electron scattering opacity accounting for the induced scattering is

$$\sigma(x, \mu) = \kappa_e \frac{1}{x} \int_0^\infty x_1 dx_1 \int_{-1}^1 d\mu_1 R(x_1, \mu_1; x, \mu) \left( 1 + \frac{C I(x_1, \mu_1)}{x_1^3} \right), \quad (12)$$

and

$$C = \frac{1}{2m_e} \left( \frac{h}{m_e c^2} \right)^3. \quad (13)$$

The source function is a sum of the thermal part and the scattering part

$$S(x, \mu) = \frac{k(x)}{\sigma(x, \mu) + k(x)} B_x + \frac{\kappa_e}{\sigma(x, \mu) + k(x)} \times \left( 1 + \frac{C I(x, \mu)}{x^3} \right) x^2 \int_0^\infty \frac{dx_1}{x_1^2} \int_{-1}^1 d\mu_1 R(x, \mu; x_1, \mu_1) I(x_1, \mu_1), \quad (14)$$

where

$$B_x = B_\nu \frac{d\nu}{dx} = \frac{x^3}{C} \frac{1}{\exp(x/\Theta) - 1}, \quad (15)$$

with  $B_\nu$  being the Planck function and

$$\Theta = \frac{kT}{m_e c^2} \quad (16)$$

the electron temperature.

The RF  $R(x, \mu; x_1, \mu_1)$  describes the probability that a photon with the dimensionless energy  $x_1$  propagating in the direction corresponding to  $\mu_1$  is scattered to energy  $x$  and in a direction corresponding to  $\mu$ . This function is found by integrating over the azimuthal angle  $\varphi$  of the RF  $R(x, x_1, \eta)$ , which depends on the cosine of the angle between the directions of the photon propagation before and after scattering  $\eta$

$$R(x, \mu; x_1, \mu_1) = \int_0^{2\pi} R(x, x_1, \eta) d\varphi, \quad (17)$$

$$\eta = \mu\mu_1 + \sqrt{1 - \mu^2} \sqrt{1 - \mu_1^2} \cos \varphi.$$

The RF depends on the depth  $s$  through the electron temperature and satisfies the relation (see Eq. A.7)

$$R(x_1, \mu_1; x, \mu) = R(x, \mu; x_1, \mu_1) \exp\left(\frac{x - x_1}{\Theta}\right), \quad (18)$$

which is the consequence of the detailed balance relation (Pomraning 1973; Nagirner & Poutanen 1994, see Appendix A). This implies that the source function given by Eq. (14) equals the Planck function for the photon field described by the Bose-Einstein distribution of any chemical potential.

In this paper, we use two RFs for Compton scattering. The first one is the fully relativistic exact RF valid for any photon energy and electron temperature (Aharonian & Atoyan 1981; Nagirner & Poutanen 1993, 1994; Poutanen & Svensson 1996, see Eqs. A.18 and A.22 in Appendix A.2). The second one is an approximate RF corresponding to the isotropic scattering in the electron rest frame (Eq. A.26 in Appendix A.2), which is accurate at temperatures below about 100 keV and non-relativistic photon energies (Arutyunyan & Nikogosyan 1980; Poutanen 1994; Poutanen & Svensson 1996). In both cases, we also consider the angle-averaged RFs

$$R(x, x_1) = \frac{1}{2} \int_{-1}^{+1} d\eta R(x, x_1, \eta), \quad (19)$$

substituting it instead of the angle-dependent RF into Eq. (17).

The formal solution of the radiation transfer equation (10) is obtained using the short-characteristic method (Olson & Kunasz 1987) in three angles in each hemisphere, and the full solution is found with an accelerated  $\Lambda$ -iteration method (see details in Appendix B).

The radiation pressure acceleration  $g_{\text{rad}}$  is computed using the RF as

$$g_{\text{rad}} = \frac{dP_{\text{rad}}}{dm} = \frac{2\pi}{c} \frac{d}{dm} \int_0^\infty dx \int_{-1}^{+1} \mu^2 I(x, \mu) d\mu \quad (20)$$

$$= \frac{2\pi}{c} \int_0^\infty dx \int_{-1}^{+1} [\sigma(x, \mu) + k(x)] [I(x, \mu) - S(x, \mu)] \mu d\mu,$$

where the derivative with respect to  $m$  is replaced by the first moment of the radiation transfer equation (10). When the source

functions and the opacities are isotropic, this expression is reduced to the standard definition

$$g_{\text{rad}} = \frac{4\pi}{c} \int_0^\infty [\sigma(x) + k(x)] H_x(m) dx, \quad (21)$$

where

$$H_x = \frac{1}{2} \int_{-1}^{+1} \mu I(x, \mu) d\mu \quad (22)$$

is the first moment of specific intensity.

These equations are completed by the energy balance equation

$$\int_0^\infty dx \int_{-1}^{+1} [\sigma(x, \mu) + k(x)] [I(x, \mu) - S(x, \mu)] d\mu = 0, \quad (23)$$

the ideal gas law

$$P_g = N_{\text{tot}} kT, \quad (24)$$

where  $N_{\text{tot}}$  is the number density of all particles, and the particle and charge conservation equations. In our calculations, we assumed local thermodynamic equilibrium (LTE), therefore the number densities of all ionization and excitation states of all elements were calculated using the Boltzmann and Saha equations. We accounted for the pressure ionization effects on hydrogen and helium populations using the occupation probability formalism (Hummer & Mihalas 1988) as described by Hubeny et al. (1994). In addition to electron scattering, we took into account the free-free opacity as well as the bound-free transitions for all ions of the 15 most abundant chemical elements (H, He, C, N, O, Ne, Na, Mg, Al, Si, S, Ar, Ca, Fe, Ni) (see Ibragimov et al. 2003) using opacities from Verner & Yakovlev (1995).

## 2.2. Method of solution

To solve the above equations, we used our version of the computer code ATLAS (Kurucz 1970, 1993), modified to deal with high temperatures (Suleimanov & Poutanen 2006; Suleimanov & Werner 2007). The code was further developed to account for Compton scattering using the RF approach.

In our computations, we used 300–360 logarithmically equidistant frequency points in the range  $10^{14}$ – $10^{20}$  Hz ( $\approx 4 \times 10^{-4}$ – $400$  keV) for the luminous model atmospheres ( $l \geq 0.1$ ), and  $10^{14}$ – $10^{19}$  Hz for  $l < 0.1$ . The calculations were performed at a set of 98 depth points  $m_i$  distributed equidistantly on the logarithmic scale from  $10^{-6}$  to  $m_{\text{max}} = 10^6$  g cm $^{-2}$ . The appropriate value of  $m_{\text{max}}$  was chosen to satisfy the condition  $\sqrt{\tau_{\nu, \text{b-f, f-f}}(m_{\text{max}}) \tau_{\nu}(m_{\text{max}})} > 1$  at all frequencies, where  $\tau_{\nu, \text{b-f, f-f}}$  is the optical depth computed with the true opacity only (bound-free and free-free transitions, without scattering). This requirement was necessary for satisfying the inner boundary condition of the radiation transfer problem.

The course of the calculations was the same as for the method that adopts the Kompaneets operator (SPW11). First, a starting grey atmosphere model was calculated and opacities at all depth points and all frequencies were obtained. The solution of the radiative transfer equation (10) was checked for the energy balance equation (23), together with the surface flux condition

$$4\pi \int_0^\infty H_x(m=0) dx = 4\pi H_0 = \sigma_{\text{SB}} T_{\text{eff}}^4. \quad (25)$$

The relative flux error

$$\varepsilon_H(m) = 1 - \frac{H_0}{\int_0^\infty H_x(m) dx}, \quad (26)$$

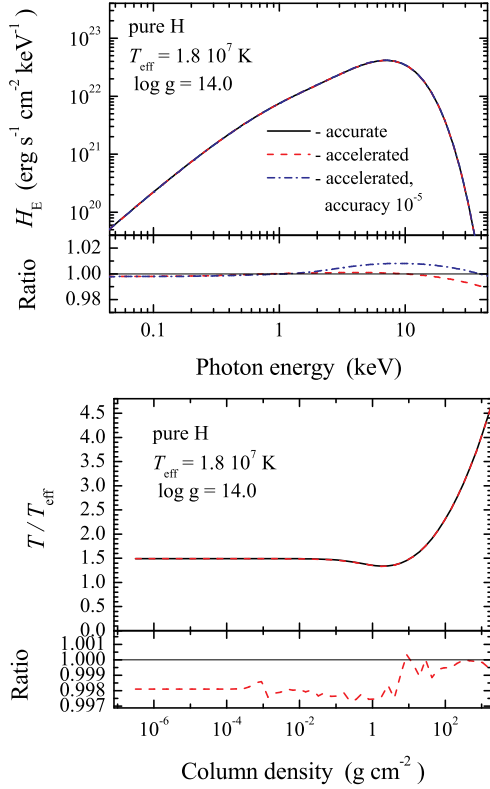


**Fig. 1.** Emergent spectrum (*top panel*) and temperature structure (*bottom panel*) of the fiducial model (pure hydrogen,  $T_{\text{eff}} = 1.8 \times 10^7$  K,  $\log g = 14.0$ ) computed using three different methods. In accurate method 1 every  $\Lambda$ -iteration starts from the thermal part of the source function (solid curves give the results for the relative accuracy of  $10^{-4}$ ). In accelerated method 2, the  $\Lambda$ -iterations start from the source function taken from previous temperature iteration, but at every fifth temperature correction they start from the thermal part of the source function (dashed curves show results for the relative accuracy of  $10^{-4}$ ). Method 3 is the same as method 2, but for the relative accuracy of  $10^{-5}$  (dot-dashed curve). In the *top lower panel*, the ratios of the spectra for methods 2 and 3 to the spectrum computed with method 1 are shown. The ratio of the temperature structures computed using methods 2 and 1 is shown in the *bottom lower panel*.

and the energy balance error

$$\varepsilon_{\Lambda}(m) = \frac{1}{2} \int_0^{\infty} dx \int_{-1}^{+1} [\sigma(x, \mu) + k(x)] [I(x, \mu) - S(x, \mu)] d\mu \quad (27)$$

were calculated as functions of depth. Temperature corrections were then evaluated using three different procedures. In the upper atmospheric layers, we used the integral  $\Lambda$ -iteration method, modified for Compton scattering, based on the energy balance equation (23). The temperature correction for a particular depth was found as

$$\Delta T_{\Lambda} = -\varepsilon_{\Lambda}(m) \left( \int_0^{\infty} \left[ \frac{\Lambda_d(x) - 1}{1 - \alpha(x)\Lambda_d(x)} \right] k(x) \frac{dB_x}{dT} dx \right)^{-1}, \quad (28)$$

where  $\alpha(x) = \sigma_{\text{CS}}(x)/(k(x) + \sigma_{\text{CS}}(x))$ , and  $\Lambda_d(x)$  is the diagonal matrix element of the  $\Lambda$ -operator. Here  $\sigma_{\text{CS}}(x)$  is the Compton scattering opacity averaged over the relativistic Maxwellian electron distribution (see Eq. (A16) in Poutanen & Svensson

1996, which is equivalent to Eq. (12) if one ignores the induced scattering). In the deep layers, we used the Avrett-Krook flux correction based on the relative flux error  $\varepsilon_H(m)$ . Finally, the third procedure was the surface correction based on the emergent flux error (see Kurucz 1970 for a detailed description of the methods).

The iteration procedure is repeated until the relative flux error is smaller than 0.1%, and the relative flux derivative error is smaller than 0.01%. As a result, we obtain a self-consistent NS model atmosphere, together with the emergent spectrum of radiation. We note that this accuracy is unachievable for luminous models with  $g_{\text{rad}} \approx g$ , and that these models can have larger relative flux errors, up to 2–3%.

### 2.3. Accuracy of computation

To compute a new extended set of hot NS model atmospheres, we accelerated the convergence of the iterations of the radiation transfer equation by using the source function from the previous temperature iteration as the first approximation (see Appendix B). However, in every fifth temperature iteration the radiation transfer equation was solved using the pure thermal source function as a first approximation. We compared a pure hydrogen model atmosphere computed for  $T_{\text{eff}} = 1.8 \times 10^7$  K and  $\log g = 14.0$  (the fiducial model) using this accelerated approach with the model computed without acceleration. The temperature structures differ by less than 0.3%, and the differences between the emergent spectra are about 1% in the 3–20 keV energy range (typical of *RXTE/PCA*) and larger in the Wien tail (Fig. 1).

As a convergence criterion for the solution of the radiation transfer equation, we chose the maximum relative error of  $10^{-4}$  in the mean intensity at all depths and energies. To determine the uncertainty in the final spectrum caused by this criterion, we compared the emergent spectra computed for the same model atmosphere with the accuracies of  $10^{-4}$  and  $10^{-5}$  (see *top panel* of Fig. 1). We see that the relative error is smaller than 1% at all energies, which is then the intrinsic accuracy of our model spectra. We note that a similar error is introduced into the angular dependence of the specific intensities by ignoring polarization (see e.g. Chandrasekhar 1960, compare his Tables XV and XXIV).

### 2.4. Various RFs and the Kompaneets operator

A comparison of model atmospheres, which were computed using our new code with four different RFs (exact angle-dependent, exact angle-averaged, approximate angle-dependent, and approximate angle-averaged) is shown in the left panels of Fig. 2. The model computed using the approximate angle-dependent RF is almost indistinguishable from the reference model calculated using the exact angle-dependent RF. This is unsurprising, because the approximate function matches the accurate one very well up to the temperatures of about 100 keV. Similar results were obtained by Poutanen & Svensson (1996) for the Comptonization spectra in the optically thin slabs. The differences are smaller than 1% for the emergent spectra and below 0.3% for the temperature structure. Deviations of model atmospheres computed using the angle-averaged RF of the reference model are more significant, at about 2% for both the temperature structure and spectra.

The model atmosphere calculated employing the Kompaneets operator has more significant differences from the reference model (see right panels in Fig. 2), of up to 10% in the temperature structure and about 3–4% in the emergent flux

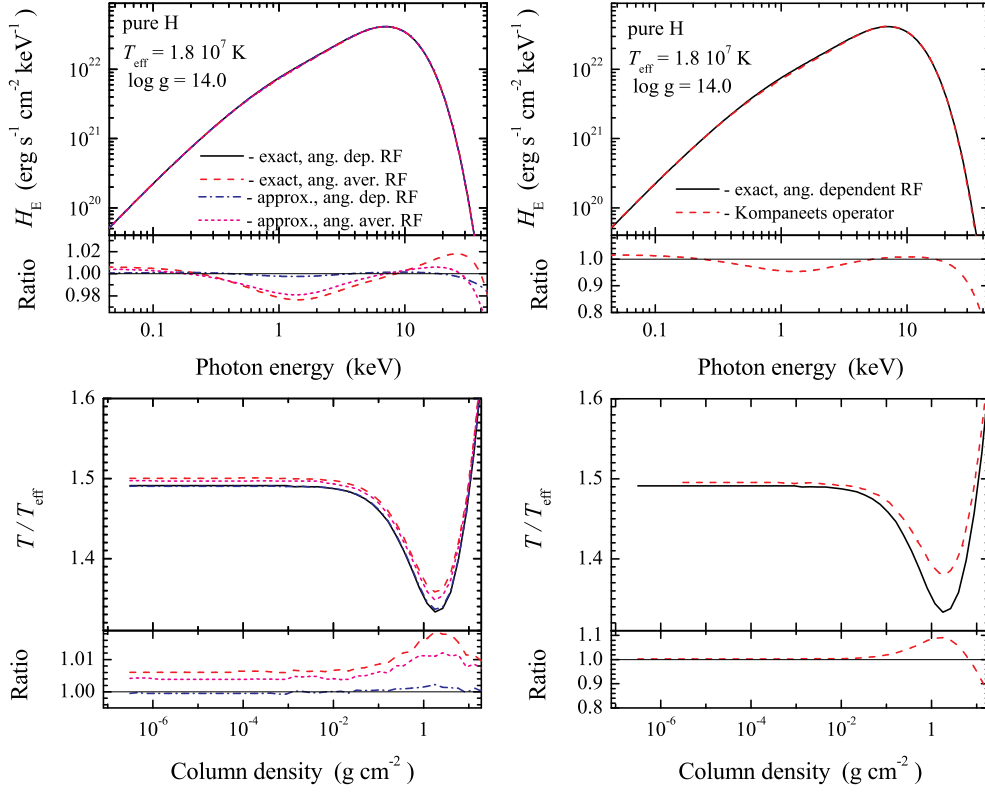


**Fig. 2.** *Left panels* present the emergent spectrum (*top panel*) and the temperature structure (*bottom panel*) of the fiducial model computed using four different RFs: (a) exact angle-dependent (solid curves), (b) exact angle-averaged (dashed curves), (c) approximate angle-dependent (dot-dashed curves), and (d) approximate angle-averaged (dotted curves). In the *top lower sub-panel*, the ratios of the spectra (b), (c), and (d) to the spectrum for case (a) are shown. In the *bottom lower sub-panel*, the ratio of the temperature structures (b), (c), and (d) to that of case (a) are shown. *Right panels* present the emergent spectrum (*top panel*) and the temperature structure (*bottom panel*) of the fiducial model computed using an exact angle-dependent RF (solid curves) and the Kompaneets operator (dashed curves).

at 1 keV. The deviations are much smaller ( $< 1\%$ ) near the spectral maximum and larger in the Wien tail. A rather good agreement between model atmospheres computed with the relativistic exact angle-dependent RF and the non-relativistic angle-independent Kompaneets operator again is unsurprising, because temperatures of the upper atmosphere layers where the emergent spectra form are sufficiently low ( $\sim 2\text{--}4$  keV) and relativistic corrections are small.

### 3. New grid of models

#### 3.1. General properties

We computed a new set of hot NS model atmospheres using the exact relativistic angle-dependent RF. The models were calculated for six chemical compositions (pure hydrogen, pure helium, and solar hydrogen/helium mix with various heavy element abundances: of solar and 0.3, 0.1 and 0.01 of solar). For every chemical composition, 26–28 models with relative luminosities spanning the interval from  $l = 0.001$  to 1.06–1.10 for three values of the surface gravity ( $\log g = 14.0, 14.3$  and 14.6) were calculated. Because the radiative acceleration in our models is smaller than in the models based on the Thomson opacity owing to the Klein-Nishina reduction in the cross-section (see below), there exist formally “super-Eddington” (relative to  $L_{\text{Edd}}$ ) models. The Klein-Nishina reduction depends on the electron

temperature, which is higher for larger surface gravities, therefore the limiting luminosity is higher for larger  $\log g$ .

Examples of emergent spectra and temperature structures for the models with  $\log g = 14.0$  and various chemical compositions (pure hydrogen and solar mix) are shown in Fig. 3.<sup>1</sup> The corresponding emergent spectra and temperature structures computed with the old code employing the Kompaneets operator are also shown. At low luminosities, the models are very close to each other, which is expected as at low temperatures the diffusion (Kompaneets) approximation is an accurate representation of Compton scattering. For models close to the Eddington limit, the treatment of the radiative acceleration becomes important. Contribution of the radiation force to the hydrostatic equilibrium  $g_{\text{rad}}/g$  is smaller in the new models despite  $l$  being the same for both model sets. It is well-known that the model spectra with large contributions of radiative acceleration are harder, and their surface temperatures are higher (London et al. 1986; Lapidus et al. 1986; Ebisuzaki 1987; Pavlov et al. 1991). In complete agreement with this, the old models with large  $l$  are harder and hotter than new models. However, for the same  $g_{\text{rad}}/g$  the new model spectra are hotter. Normalizing the spectra to the maximum flux and plotting them against the scaled photon en-

<sup>1</sup> The spectral energy distributions of fluxes and specific intensities for all models are described in Appendix D.

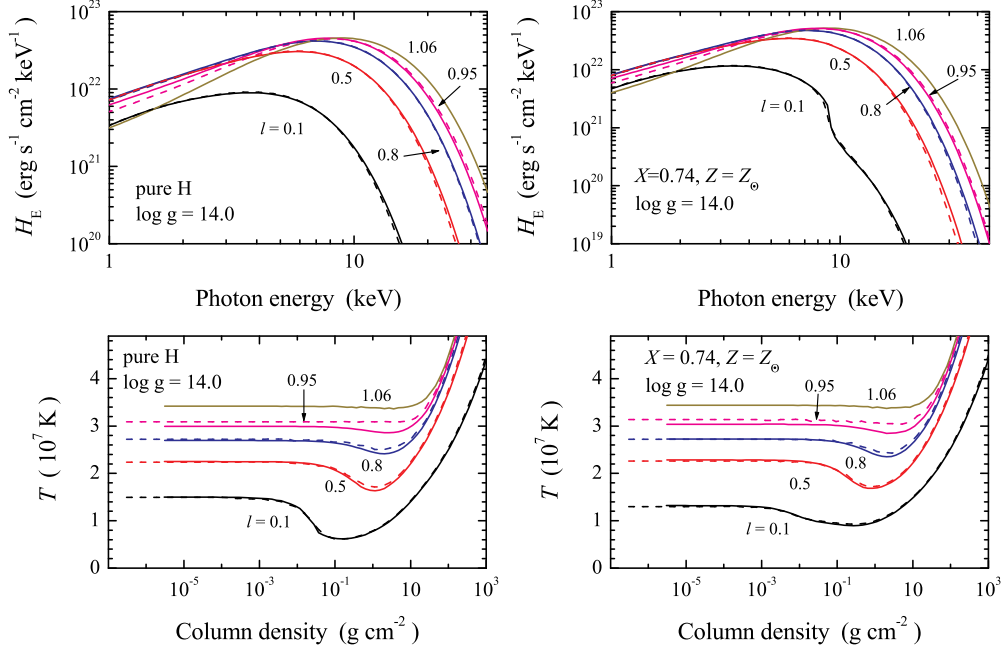


**Fig. 3.** Comparison of the emergent spectra (*top panel*) and the temperature structures (*bottom panel*) computed using the present code with the exact RF (solid curves) and the previous code employing the Kompaneets operator (dashed curves). The models for various relative luminosities are marked by corresponding numbers next to the curves. *Left panels* are for pure H and *right panels* are for the solar abundances.

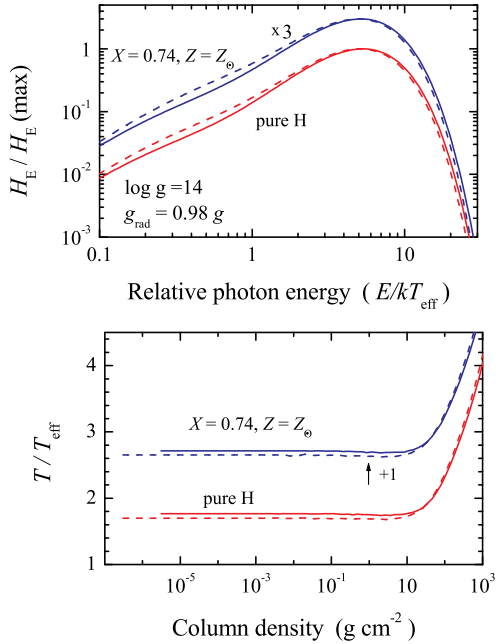


**Fig. 4.** Comparison of the emergent spectra (*top panel*) and the temperature structures (*bottom panel*) of the new (solid curves) and the old (dashed curves) models with the same  $g_{\text{rad}}/g$ . The models are computed for pure hydrogen as well as solar abundance. The models have different effective temperatures, therefore the spectra are normalized to the maximum flux and plotted against the scaled photon energy. For clarity, the spectra of solar abundance models are shifted by a factor of three, and the relative temperatures are shifted by adding one.

ergies  $E/kT_{\text{eff}}$ , one also sees that the new spectra are harder (see Fig. 4).

### 3.2. Limb-darkening

Knowledge of the angular distribution of the emergent radiation is important when only part of the star is visible (for example, is partially blocked by the accretion disk), or when there are inhomogeneities at the NS surface related, for example, to the varying gravitational acceleration due to the rapid rotation. Computation of the amplitude of reflection from the accretion disk also requires that information. The limb-darkening law (i.e. angular dependence of the intensity) for the radiation emerging from the optically thick electron-scattering-dominated atmosphere is described by the  $H^{(0)}(\mu)$  function (Chandrasekhar & Breen 1947; Chandrasekhar 1960; Sobolev 1949, 1963). A simple approximation to this function is  $I(\mu) \approx 1 + 2.06\mu$ . Our simulations show that the intensity closely (within a couple of per cents) follows the  $H^{(0)}(\mu)$  function around the peak of the spectrum, in the observed energy range (see Fig. 5). At photon energies below 1 keV, the computed angular distribution becomes more isotropic, because there free-free absorption dominates over electron scattering and the upper atmosphere layers are almost isothermal. The low-inclination intensity is above and the high-inclination intensity is below the electron-scattering limb-darkening law at energies above the peak, because the temperature of the layer where the photons originate drops with the inclination. The iron absorption edge at  $\sim 9$  keV significantly affects the angular distribution for the solar abundance models (Fig. 5, *bottom panel*). Above the edge, radiation becomes more directed along the surface normal.

The angular distribution of the intensity also depends on the specific form of the RF used in the calculations. The approximate angle-dependent gives results very close to the reference

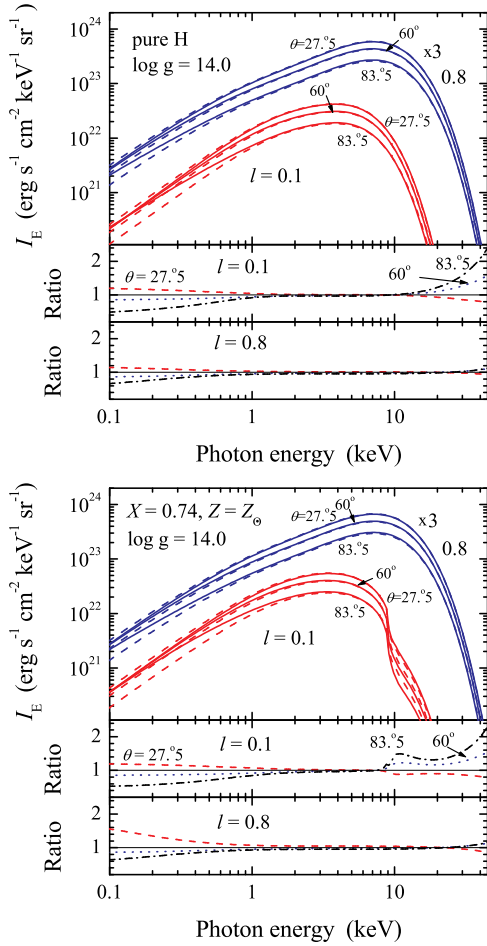


**Fig. 5.** Comparison of the emergent specific intensity for pure hydrogen (*top panel*) and solar abundance models (*bottom panel*) with the electron-scattering limb-darkening law (dashed curves) for two relative luminosities of  $l = 0.1$  and  $0.8$ . The  $l = 0.8$  models are multiplied by a factor of three for clarity. The lower sub-panels show the ratios of the corresponding models.

intensity spectra, within 2% for the largest angle  $\theta$  (see Fig. 6, *top panel*). The exact, but angle-averaged, RF, does not give such accurate results (see Fig. 6, *bottom panel*).

### 3.3. Color correction factors

All computed emergent spectra of the new atmosphere models were fitted by a diluted blackbody spectrum

$$F_E \approx w B_E(f_c T_{\text{eff}}) \quad (29)$$

using five different fitting procedures described in SPW11. We calculated the color correction  $f_c$  and dilution  $w$  factors in the energy band  $(3-20) \times (1+z)$  keV corresponding to the observed range of the *RXTE/PCA* detector. We calculated redshifts from  $\log g$  by adopting a NS mass equal to  $1.4 M_\odot$  (see Eqs. (1) and (4)): for  $\log g = 14.0, 14.3,$  and  $14.6$ , we get  $R = 14.80, 10.88, 8.16$  km and  $z = 0.18, 0.27, 0.42$ , respectively. Varying the mass in the interval  $1-2 M_\odot$  has a smaller than 0.1% effect on the color corrections (SPW11). The results of the fitting procedures are presented in Table 1 (see also Appendix D).

Deviations of the new model spectra from the best-fit diluted blackbodies are similar to those for the old spectra based on the

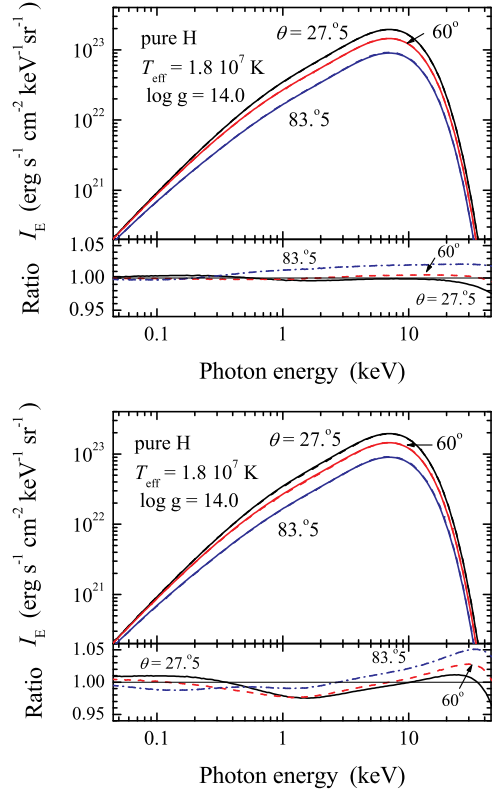


**Fig. 6.** Comparison of the emergent specific intensity at three angles (from the Gaussian quadrature  $\mu = 0.113, 0.5, 0.887$ , i.e.  $\theta = 83.5^\circ, 60^\circ, 27.5^\circ$ ) for the fiducial model computed using the exact angle-dependent RF (solid curves in both panels) with the spectra based on the approximate angle-dependent RF (*top panel*, dashed curves) and exact angle-averaged RF (*bottom panel*, dashed curves). In the bottom sub-panels, the ratios of the accurate spectra to the approximate spectra for the three angles are shown.

Kompaneets operator (Fig. 7). Comparison of the new and old color correction factors is shown in Figs. 8 and 9. Although the old  $f_c-l$  dependences for different gravities were almost identical at high luminosities, we see that now these dependences deviate, because of the dependence of the limiting relative luminosity on  $\log g$ . However, the old and new color-correction factors have very similar dependences on  $g_{\text{rad}}/g$  for all  $\log g$  and chemical compositions (see Figs. 8 and 9), with the new  $f_c$  being about 1% larger. The difference grows at  $g_{\text{rad}}/g$  close to unity.

Pavlov et al. (1991) derived an approximate analytical formula for the ratio of the surface model atmosphere temperature to the effective one

$$\frac{T_{\text{surf}}}{T_{\text{eff}}} \approx \left( 0.14 \ln \frac{3+5X}{1-l} + 0.59 \right)^{-4/5} \left( \frac{3+5X}{1-l} \right)^{2/15} l^{3/20}, \quad (30)$$

which is correct for the highly luminous ( $l > 0.9$ ) model atmospheres. The numerical constants 0.14 and 0.59 were found from the fitting of their model atmospheres based on the Kompaneets operator description of Compton scattering. If the models were instead computed using an exact RF for Compton scattering, it is obvious that  $l$  should be substituted by the relative radiation acceleration  $g_{\text{rad}}/g$ . We fit our color correction factors computed using the first fitting procedure (see SPW11) with a formula similar to Eq. (30) and found numerical constants that also depend

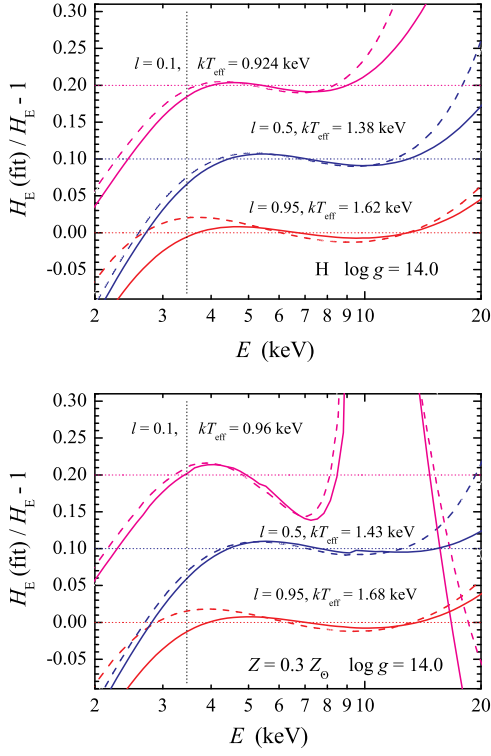


**Fig. 7.** Relative deviations of the new, exact RF-based (solid curves) and old Kompaneets-based (dashed curves) spectra from the best-fit diluted blackbodies versus photon energy for hydrogen (*top panel*) and solar H/He mixture with  $Z = 0.3Z_{\odot}$  (*bottom panel*) low gravity ( $\log g = 14.0$ ) models. Corresponding relative luminosities and the effective temperatures are given at the curves. The vertical dotted line shows the lower boundary of the energy band, where the fitting procedures were performed. For clarity, models with  $l = 0.1$  and  $0.5$  are shifted up by  $0.2$  and  $0.1$ , respectively.

on the chemical composition

$$f_c \approx \left( [0.102 + 0.008X] \ln \frac{3 + 5X}{1 - g_{\text{rad}}/g} + 0.63 - 0.06X \right)^{-4/5} \times \left( \frac{3 + 5X}{1 - g_{\text{rad}}/g} \right)^{2/15} (g_{\text{rad}}/g)^{3/20}. \quad (31)$$

This approximation works well for  $g_{\text{rad}}/g > 0.8$  (see Fig. 10).

### 3.4. Radiative acceleration

The radiative acceleration can formally be represented as a product of the flux and the temperature-dependent effective opacity

$$g_{\text{rad}} = \kappa(T) \frac{\sigma_{\text{SB}} T_{\text{eff}}^4}{c}. \quad (32)$$

This expression can alternatively be written as

$$\frac{g_{\text{rad}}}{g} = l \frac{\kappa(T)}{\kappa_e}. \quad (33)$$

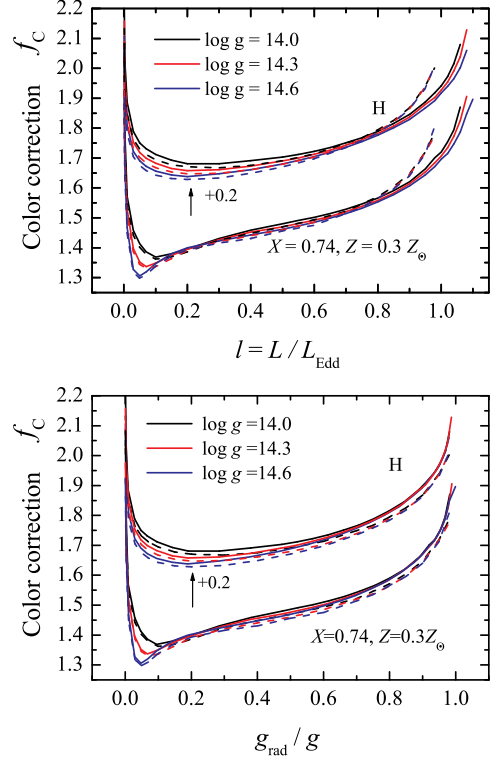


**Fig. 8.** Color correction factors  $f_{c,1}$  (computed using method 1 from SPW11) for model atmospheres of two chemical compositions (pure hydrogen and solar hydrogen/helium mix with 30% of solar heavy-element abundance) and different  $\log g$  as functions of the relative luminosity  $l$  (*top panel*) or  $g_{\text{rad}}/g$  (*bottom panel*). The new models based on the exact RF are shown by the solid curves, and the old models, based on the Kompaneets operator, by dashed curves.

In diffusion approximation,  $\kappa(T)$  is given by the Rosseland mean opacity. When electron scattering dominates, it is often approximated (neglecting the electron degeneracy) as (Paczynski 1983)

$$\kappa(T) = \kappa_{\text{R}}(T) \approx \kappa_e \left[ 1 + \left( \frac{kT}{38.8 \text{ keV}} \right)^{0.86} \right]^{-1}. \quad (34)$$

This approximation is based on calculations by Buchler & Yueh (1976), who underestimated the opacity at low temperatures, where certain approximations were made because of severe numerical problems. A better approximation in the range 2–50 keV that is of interest here is (J. Poutanen et al., in preparation)

$$\kappa_{\text{R}}(T) \approx \kappa_e \left[ 1 + \left( \frac{kT}{39.4 \text{ keV}} \right)^{0.976} \right]^{-1}. \quad (35)$$

It is clear that the radiative acceleration decreases in the deep, hotter atmosphere layers and the ratio of radiation pressure force to the surface gravity decreases inwards (see Fig. 11). The radiative acceleration is smaller than that corresponding to the Thomson opacity, even in the upper atmosphere layers. The actual radiative acceleration in the surface layers (see *top panel* in Fig. 11) computed from the models using Eq. (20) is perfectly described by Eqs. (35) and (33) throughout the whole atmosphere (compare dotted and solid curves at the *top panel* in Fig. 11), while Paczynski's approximation underestimates it.



**Table 1.** Color-correction and dilution factors from the blackbody fits to the spectra of hydrogen atmosphere models at  $\log g = 14.0$ .

Set	$X = 1$	$Z = 0$	$\log g = 14.0$	$T_{\text{Edd}} = 1.644 \text{ keV}$			$R = 14.80 \text{ km}$		$z = 0.18$		
	$l$	$g_{\text{rad}}/g$	$T_{\text{eff}} \text{ (keV)}$	$f_{c,1}$	$f_{c,2}$	$f_{c,3}$	$f_{c,4}$	$f_{c,5}$	$w_1 f_{c,1}^4$	$w_2 f_{c,2}^4$	$w_3 f_{c,3}^4$
1	0.001	0.001	0.292	2.015	2.009	2.018	1.806	1.571	0.698	0.704	0.695
1	0.003	0.003	0.385	1.830	1.826	1.833	1.662	1.473	0.796	0.800	0.794
1	0.010	0.009	0.520	1.686	1.682	1.687	1.553	1.382	0.877	0.878	0.876
1	0.030	0.028	0.684	1.589	1.587	1.589	1.525	1.375	0.926	0.926	0.926
1	0.050	0.048	0.777	1.550	1.550	1.550	1.531	1.407	0.942	0.942	0.942
1	0.070	0.067	0.845	1.531	1.530	1.530	1.533	1.431	0.949	0.949	0.949
1	0.100	0.096	0.924	1.512	1.511	1.511	1.528	1.451	0.954	0.954	0.954
1	0.150	0.143	1.023	1.493	1.492	1.492	1.512	1.462	0.963	0.962	0.963
1	0.200	0.190	1.099	1.481	1.479	1.481	1.505	1.464	0.960	0.959	0.960
1	0.300	0.285	1.217	1.481	1.476	1.480	1.500	1.478	0.971	0.969	0.971
1	0.400	0.380	1.307	1.491	1.486	1.491	1.511	1.500	0.972	0.970	0.972
1	0.500	0.474	1.382	1.503	1.497	1.503	1.521	1.515	0.974	0.972	0.974
1	0.550	0.521	1.416	1.512	1.506	1.512	1.530	1.526	0.975	0.972	0.975
1	0.600	0.567	1.447	1.522	1.516	1.522	1.539	1.538	0.977	0.973	0.976
1	0.650	0.614	1.476	1.535	1.530	1.535	1.551	1.553	0.979	0.976	0.979
1	0.700	0.661	1.504	1.551	1.546	1.551	1.566	1.569	0.981	0.977	0.980
1	0.730	0.707	1.530	1.568	1.563	1.567	1.583	1.586	0.982	0.979	0.982
1	0.800	0.733	1.555	1.589	1.586	1.588	1.600	1.608	0.985	0.983	0.984
1	0.850	0.799	1.578	1.615	1.613	1.613	1.624	1.634	0.987	0.986	0.987
1	0.900	0.844	1.601	1.646	1.648	1.644	1.653	1.665	0.992	0.993	0.991
1	0.950	0.890	1.623	1.687	1.694	1.682	1.690	1.705	0.997	1.001	0.996
1	0.980	0.917	1.635	1.718	1.729	1.712	1.718	1.735	1.000	1.007	0.999
1	1.000	0.934	1.644	1.741	1.756	1.733	1.739	1.757	1.002	1.011	1.000
1	1.020	0.952	1.652	1.772	1.793	1.762	1.767	1.787	1.006	1.018	1.003
1	1.040	0.969	1.660	1.815	1.844	1.803	1.807	1.828	1.010	1.026	1.007
1	1.060	0.981	1.668	1.880	1.921	1.864	1.869	1.888	1.012	1.036	1.009

**Notes.** Results for other chemical compositions and gravities are given in Table D.1 available in electronic form at the Centre de Données astronomiques de Strasbourg (CDS).

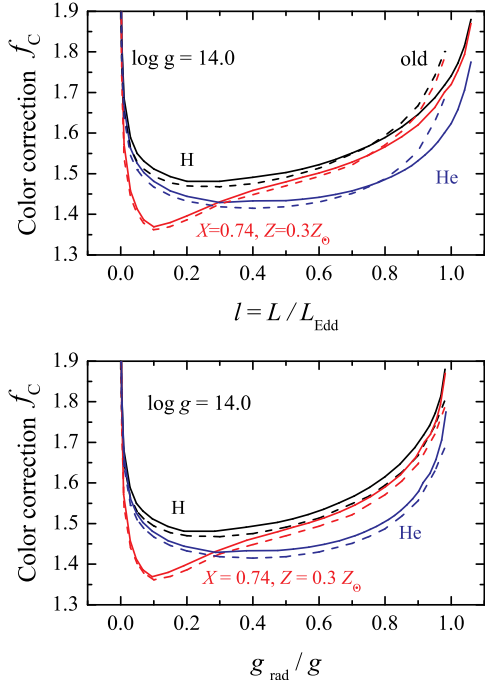


**Fig. 9.** Same as Fig. 8, but for different chemical compositions and  $\log g = 14.0$ .

Radiative acceleration computed using the angle-averaged RFs is larger than that computed using angle-dependent RFs (see

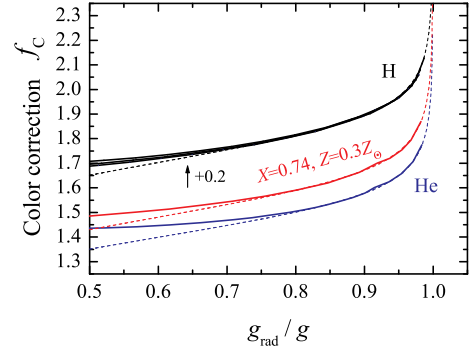


**Fig. 10.** Color correction factor  $f_c$  versus  $g_{\text{rad}}/g$  for models of various chemical compositions. Solid curves are the results of calculations based on the exact Compton RF, the dotted curves give the approximation (31). For clarity, the curves for pure H models (shown for three  $\log g$ ) are shifted up by +0.2.

bottom panel in Fig. 11), because the high-energy photons scatter on the relatively cold electrons in a predominantly forward direction, reducing the magnitude of the momentum transfer in comparison with the isotropic case.

Radiative acceleration in the surface layers that we obtain from the models can be expressed through  $T_{\text{eff}}$  and  $f_c$  as

$$\kappa(T = f_c T_{\text{eff}}) = \kappa_e \left[ 1 + \left( \frac{kT}{38.8 \text{ keV}} \right)^{\alpha_g} \right]^{-1}, \quad (36)$$

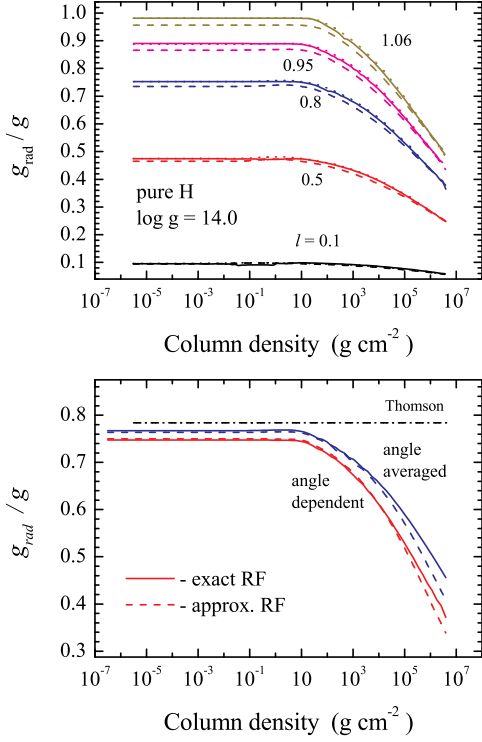


**Fig. 11.** *Top panel:* Comparison of the relative radiative acceleration in pure hydrogen atmospheres (solid curves) with our approximation given by Eq. (35) (dotted curves, which nearly coincide with solid curves) and with Paczynski’s approximation (34) (dashed curves). *Bottom panel:* Comparison of the relative radiative acceleration for the fiducial model computed with different RFs: exact and approximate, angle-dependent, and angle-averaged. The relative radiative acceleration for Thomson scattering is also shown.

where  $\alpha_g = 1.01 + 0.067(\log g - 14.0)$  (see Fig. 12). The relation  $g_{\text{rad}}/g-l$  also slightly depends on the chemical composition, but the dependence on the surface gravity is stronger.

The relation of the effective temperature to the effective opacity given by Eq. (36) allows us to estimate  $g_{\text{rad}}/g$  for the given model parameters ( $l, T_{\text{eff}}$ ) without actually computing the atmosphere models. We can make a first guess of  $f_c$ , substitute  $T = f_c T_{\text{eff}}$  to Eq. (36), then use this  $\kappa$  in Eq. (33), find a new  $f_c$  through Eq. (31), and iterate.

#### 4. Application to observations

In our previous works (S11 and SPW11), we suggested a new method for the determination of NS radii and masses. It is based on the spectral (blackbody) normalization  $K$  at late phases of PRE X-ray bursts depending on the color correction factor only

$$K \equiv \left( \frac{R_{\text{bb}}(\text{km})}{D_{10}} \right)^2 = \frac{1}{f_c^4} \left( \frac{R(\text{km})(1+z)}{D_{10}} \right)^2 = (A f_c)^{-4}, \quad (37)$$

where  $D_{10} = D/10 \text{ kpc}$  is the distance. The observed relation  $K^{-1/4}-F_{\text{bb}}$  between the blackbody flux  $F_{\text{bb}}$  and normalization  $K$  can be fitted by the theoretical dependence  $f_c-l$  obtained from the atmosphere models. The fit gives two parameters: the value of  $A = [R(\text{km})(1+z)/D_{10}]^{-1/2}$  and the observed Eddington flux

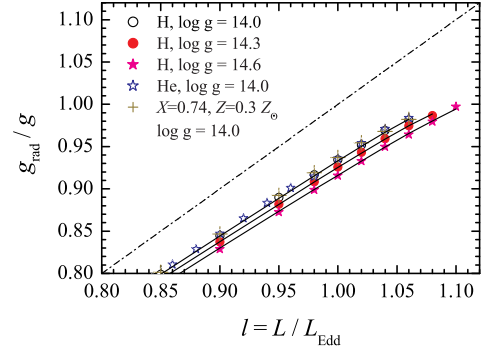


**Fig. 12.** Dependence of the relative radiative acceleration  $g_{\text{rad}}/g$  on  $l$ . Symbols represent the results of calculations based on the exact Compton RF, the solid curves give the approximation (36). The dot-dashed curve is the  $l = g_{\text{rad}}/g$  relation.

$F_{\text{Edd}} = L_{\text{Edd}}(1+z)^{-2}/(4\pi D^2)$ . The distance-dependent quantities  $A$  and  $F_{\text{Edd}}$  can be combined to the distance-independent Eddington temperature which is the apparent effective temperature corresponding to  $L_{\text{Edd}}$

$$T_{\text{Edd},\infty} = \left( \frac{gc}{\sigma_{\text{SB}}\kappa_c} \right)^{1/4} \frac{1}{1+z} = 6.4 \times 10^9 A F_{\text{Edd}}^{1/4} \text{ K}. \quad (38)$$

If the distance to the source is known (for example, for sources in globular clusters), we can plot three curves on the  $M-R$  plane corresponding to the values of  $A, F_{\text{Edd}}$ , and  $T_{\text{Edd},\infty}$ . Two crossing points give two pairs of NS mass and radius values that satisfy the observed data.

It is now important to understand how the new models affect results based on formulae that use the Thomson cross-section for electron scattering. We have seen that owing to the Klein-Nishina reduction in the cross-section, the actual Eddington limit is reached at luminosities of 6–10% higher than  $L_{\text{Edd}}$  and the shape of the  $f_c-l$  relation differs somewhat from the Kompaneets-based results. As an illustration, we consider a long PRE X-ray burst of 4U 1724–307 in the globular cluster Terzan 2 studied by S11, who obtained a rather large NS radius for this source ( $R \geq 14 \text{ km}$ ). We now use new sets of theoretical relations  $f_c-l$  that we fit to the observed relation  $K^{-1/4}-F_{\text{bb}}$ , taking pure hydrogen models as an example. We note that the new relations significantly depend on the surface gravity (see Fig. 8, *top panel*), therefore, in principle, it would be possible also to find the surface gravity that provides the best fit to the observed relation. This is, however, difficult in practise, because a change in  $\log g$  can be compensated for by varying  $F_{\text{Edd}}$ .

The theoretical  $f_c-l$  curve for  $\log g = 14.0$  gives the best fit to the data (Fig. 13) for  $A = 0.168$  and  $F_{\text{Edd}} = 4.93 \times 10^{-8} \text{ erg s}^{-1} \text{ cm}^{-2}$ . The corresponding old, Kompaneets-based values are 0.170 and  $5.25 \times 10^{-8}$ , respectively. This small change in the best-fit parameters leads to a small decrease of  $T_{\text{Edd},\infty}$  from  $1.64 \times 10^7 \text{ K}$  to  $1.60 \times 10^7 \text{ K}$  and a corresponding increase in the NS radii (see Fig. 13, *bottom panel*). Interestingly, the new  $T_{\text{Edd},\infty}$  curve crosses with the curve  $\log g = 14.0$  at the NS mass close to  $1.5M_{\odot}$ , and the curve  $A = 0.168$  also passes through the same crossing point when  $D_{10} = 0.53$  (i.e. 5.3 kpc, the distance to Terzan 2, Ortolani et al. 1997). The uncertainties in the obtained values arising owing to uncertainties in the data are very close to the differences between the old and the new values of the best-fit parameters (see Table 1 in S11).

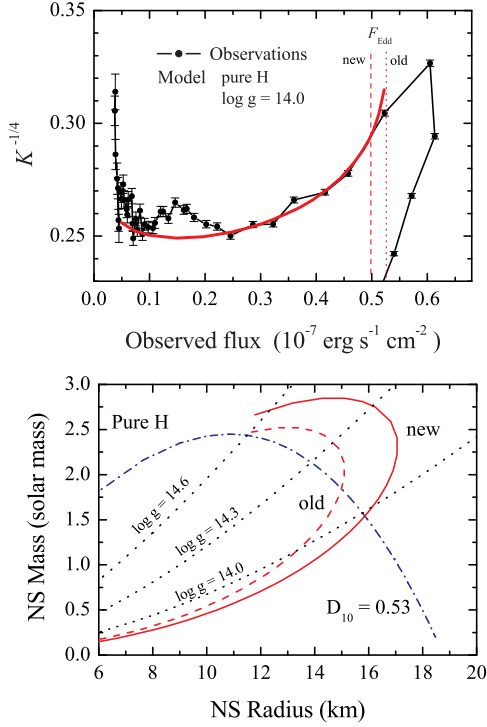


**Fig. 13.** *Top panel:* The fit of the X-ray burst data for 4U 1724–307 by the theoretical models for the NS atmosphere. The circles indicate the observed dependence of  $K^{-1/4}$  versus  $F$  for the long burst (S11) and the solid curve corresponds to the best-fit theoretical model for a pure hydrogen atmosphere and  $\log g = 14.0$ . Vertical dotted and dashed lines show the best-fit value for  $F_{\text{Edd}}$  for the old and new models. *Bottom panel:* Constraints on mass and radius of the NS in 4U 1724–307. The new (solid) and the old (dashed) curves corresponding to  $T_{\text{Edd},\infty}$  are shown. The dash-dotted curve corresponds to the new best-fit parameter  $A$  for the distance to the source of 5.3 kpc.

A few attempts to find NS mass and radius from the direct fitting of the observed X-ray burst spectrum by NS atmosphere model spectra were performed (Majczyna & Madej 2005; Miller et al. 2011; Kuśmierk et al. 2011). They have proposed finding the best fit for a fixed  $\log g$  by varying the relative luminosity  $l$  (or effective temperature  $T_{\text{eff}}$ ) and the gravitational redshift  $z$ . The best-fit between all trial  $\log g$  values then gives the desired  $\log g$  and  $z$ . Thereafter, the NS mass and radius can be found using Eqs. (1) and (4). Unfortunately, the curves on the  $M$ – $R$  plane corresponding to the fixed values of  $\log g$  and  $z$  cross at very small angles (see Fig. 1 in SPW11). Therefore, the uncertainties are expected to be large. More importantly, the model spectra are very close to the blackbody in the observed *RXTE*/*PCA* energy band. This means that for an arbitrary product  $f_c T_{\text{eff}}$  (i.e. color temperature of the theoretical spectrum) we can find the redshift  $z$  that makes the combination  $f_c T_{\text{eff}}/(1+z)$  equal to the observed color temperature  $T_{\text{bb}}$ , and in turn this method extremely unreliable.

## 5. Summary

We have considered hot NS model atmospheres taking into account Compton scattering using the relativistic kinetic equation with the exact angle-dependent RF and cross-section

(Nagirner & Poutanen 1994; Poutanen & Svensson 1996), accounting also for the induced scattering. We have developed a method to solve the obtained radiation transfer equation using a short characteristic method with the accelerated  $\Lambda$ -iteration. We have implemented this solution in our computer code for the model atmosphere calculations (SPW11).

We have examined the properties of the new model atmospheres. The main difference in comparison with the old models computed with the Kompaneets operator concerns radiative acceleration. In the new approach, the Klein-Nishina reduction in the electron scattering cross-section leads to a decrease in the radiative acceleration relative to that for the Thomson scattering cross-section. The grid of model atmospheres was extended to higher effective temperatures up to luminosities formally exceeding the Eddington limit  $L_{\text{Edd}}$  computed for the Thomson cross-section. The role of the radiation pressure reduces in the deeper, hot, optically thick layers due to the same effect.

We computed a new set of 484 hot NS model atmospheres. Following SPW11, we computed the models for six different chemical compositions (pure hydrogen, pure helium, solar hydrogen/helium mix with various abundances of heavy elements  $Z = 1, 0.3, 0.1,$  and  $0.01 Z_{\odot}$ ) and three surface gravities ( $\log g = 14.0, 14.3,$  and  $14.6$ ). The relative luminosities range from  $l=0.001$  to  $1.06$ – $1.1$  (depending on  $\log g$ ). The new models with  $l < 0.8$  are almost identical to the old models based on the Kompaneets operator approach. At higher  $l$ , the deviations are more significant due to a different treatment of the radiative acceleration. The difference between the new and old models is small if instead of  $l$  one uses the relative radiative acceleration  $g_{\text{rad}}/g$  as a parameter.

The spectra of the new and old models deviate by less than 5% in the region around the spectral peak, and the deviation grows at higher energies. We have also tested various approximate and angle-averaged RFs for Compton scattering and found that they produce spectra that deviate from the exact solution typically by less than 2%. The comparison of our spectra to the models computed using Madej’s code (Madej 1991; Madej et al. 2004; Majczyna et al. 2005) revealed dramatic differences in the spectral shape. We attribute these differences to their usage of the incorrect RF from Guilbert (1981) and/or to the non-convergence of their radiation transfer calculations.

The spectra of all our models were fitted by the diluted blackbody spectra in the *RXTE*/*PCA* energy band (3–20 keV) using the same five fitting procedures as in SPW11. The new  $f_c$ – $l$  relations are similar in shape to the old relations, but depend significantly on the surface gravity. However, the dependences of the color correction on  $g_{\text{rad}}/g$  are almost indistinguishable, with the new  $f_c$  being larger by approximately 1%. The color corrections with the corresponding dilution factors, the theoretical emergent spectral energy distributions, and specific intensities at various angles for all models are available at CDS.

In the present paper, we have also tested how the new  $f_c$ – $l$  relations affect the determination of the NS masses and radii derived from the spectral evolution observed during the cooling stages of PRE bursts. We found that the best-fit NS radius increases by about 10% from the value obtained using the old model based on the Kompaneets equation (S11). We note that bursting NSs are rapidly rotating and accounting for the latitudinal variation in gravity and the Doppler effect will affect the estimated NS radius. This will be a subject of a separate publication.

*Acknowledgements.* The work is supported by the German Research Foundation (DFG) grant SFB/Transregio 7 Gravitational Wave Astronomy, Russian Foundation for Basic Research (grant 12-02-97006-r-povolzhe-a), the Jenny ja

Antti Wihuri foundation, and the Academy of Finland (grant 127512). We also acknowledge the support of the International Space Science Institute (Bern, Switzerland), where part of this investigation was carried out. We are grateful to Jerzy Madej and Agata Rózańska for kindly providing us with the results of their atmosphere calculations.

## References

- Aharonian, F. A. & Atoyan, A. M. 1981, *Ap&SS*, 79, 321  
 Arutyunyan, G. A. & Nikogosyan, A. G. 1980, *Sov. Phys. – Dokl.*, 25, 918  
 Berestetskii, V. B., Lifshitz, E. M., & Pitaevskii, L. P. 1982, *Quantum electrodynamics* (Oxford: Pergamon Press)  
 Buchler, J. R. & Yueh, W. R. 1976, *ApJ*, 210, 440  
 Chandrasekhar, S. 1960, *Radiative transfer* (New York: Dover)  
 Chandrasekhar, S. & Breen, F. H. 1947, *ApJ*, 105, 435  
 Damen, E., Magnier, E., Lewin, W. H. G., et al. 1990, *A&A*, 237, 103  
 de Groot, S. R., van Leeuwen, W. A., & van Weert, C. G. 1980, *Relativistic kinetic equation* (Amsterdam: North-Holland)  
 Ebisuzaki, T. 1987, *PASJ*, 39, 287  
 Galloway, D. K., Muno, M. P., Hartman, J. M., Psaltis, D., & Chakrabarty, D. 2008, *ApJS*, 179, 360  
 Guilbert, P. W. 1981, *MNRAS*, 197, 451  
 Hubeny, I., Hummer, D., & Lanz, T. 1994, *A&A*, 282, 151  
 Hummer, D. & Mihalas, D. 1988, *ApJ*, 331, 794  
 Ibragimov, A. A., Suleimanov, V. F., Vikhlinin, A., & Sakhbullin, N. A. 2003, *Astronomy Reports*, 47, 186  
 Jüttner, F. 1911, *Ann. Physik und Chemie*, 34, 856  
 Kompaneets, A. S. 1957, *Sov. Phys.–JETP*, 4, 730  
 Kurucz, R. 1993, *ATLAS9 Stellar Atmosphere Programs and 2 km/s grid*. Kurucz CD-ROM No. 13, Cambridge, Mass.: Smithsonian Astrophysical Observatory  
 Kurucz, R. L. 1970, *SAO Special Report*, 309  
 Kuśmierk, K., Madej, J., & Kuulkers, E. 2011, *MNRAS*, 415, 3344  
 Lapidus, I. I., Syunyaev, R. A., & Titarchuk, L. G. 1986, *Soviet Astron. Lett.*, 12, 383  
 Lattimer, J. M. & Prakash, M. 2007, *Phys. Rep.*, 442, 109  
 Lewin, W. H. G., van Paradijs, J., & Taam, R. E. 1993, *Space Science Reviews*, 62, 223  
 London, R. A., Taam, R. E., & Howard, W. M. 1986, *ApJ*, 306, 170  
 Madej, J. 1991, *ApJ*, 376, 161  
 Madej, J., Joss, P. C., & Rózańska, A. 2004, *ApJ*, 602, 904  
 Majczyna, A. & Madej, J. 2005, *Acta Astron.*, 55, 349  
 Majczyna, A., Madej, J., Joss, P. C., & Rózańska, A. 2005, *A&A*, 430, 643  
 Mihalas, D. 1978, *Stellar atmospheres*, 2nd edition (San Francisco, W. H. Freeman and Co.)  
 Miller, M. C., Boutloukos, S., Lo, K. H., & Lamb, F. K. 2011, in *Fast X-ray timing and spectroscopy at extreme count rates*, PoS (HTRS 2011) 024  
 Nagirner, D. I. & Poutanen, J. 1993, *A&A*, 275, 325  
 Nagirner, D. I. & Poutanen, J. 1994, *Astrophys. Space Phys. Rev.*, 9, 1  
 Olson, G. L. & Kunasz, P. B. 1987, *J. Quant. Spec. Radiat. Transf.*, 38, 325  
 Ortolani, S., Bica, E., & Barbuy, B. 1997, *A&A*, 326, 614  
 Paczynski, B. 1983, *ApJ*, 267, 315  
 Pavlov, G. G., Shibanov, I. A., & Zavlin, V. E. 1991, *MNRAS*, 253, 193  
 Pomraning, G. C. 1973, *The Equations of Radiation Hydrodynamics* (Oxford: Pergamon)  
 Poutanen, J. 1994, PhD thesis, Univ. Helsinki  
 Poutanen, J. & Svensson, R. 1996, *ApJ*, 470, 249  
 Poutanen, J. & Vurm, I. 2010, *ApJS*, 189, 286  
 Prasad, M. K., Kershaw, D. S., & Beason, J. D. 1986, *Appl. Phys. Lett.*, 48, 1193  
 Sobolev, V. V. 1949, *Uch. Zap. Leningrad Univ.*, 16  
 Sobolev, V. V. 1963, *A treatise on radiative transfer* (Princeton: Van Nostrand)  
 Stern, B. E., Poutanen, J., Svensson, R., Sikora, M., & Begelman, M. C. 1995, *ApJ*, 449, L13  
 Strohmayer, T. & Bildsten, L. 2006, in *Compact stellar X-ray sources*, Cambridge Astrophysics Series, No. 39, ed. W. Lewin & M. van der Klis (Cambridge: Cambridge University Press), 113  
 Suleimanov, V. & Poutanen, J. 2006, *MNRAS*, 369, 2036  
 Suleimanov, V., Poutanen, J., Revnivtsev, M., & Werner, K. 2011a, *ApJ*, 742, 122 (S11)  
 Suleimanov, V., Poutanen, J., & Werner, K. 2011b, *A&A*, 527, A139 (SPW11)  
 Suleimanov, V. & Werner, K. 2007, *A&A*, 466, 661  
 Sygne, J. L. 1957, *The Relativistic Gas* (Amsterdam: North-Holland Publication)  
 van Paradijs, J., Dotani, T., Tanaka, Y., & Tsuru, T. 1990, *PASJ*, 42, 633  
 Verner, D. A. & Yakovlev, D. G. 1995, *A&AS*, 109, 125  
 Zdziarski, A. A., Poutanen, J., & Johnson, W. N. 2000, *ApJ*, 542, 703

## Appendix A: Relativistic kinetic equation for Compton scattering and the RFs

For completeness let us rederive here the exact relativistic expressions for the Compton scattering RFs. For the detailed derivation, see Nagirner & Poutanen (1993) and Poutanen & Vurm (2010), where more general problems have been solved. In the first paper, the redistribution matrices describing Compton scattering of polarized radiation in terms of Stokes parameters were derived, while in the second the RFs for anisotropic electron distribution have been obtained. We start from the relativistic kinetic equation (RKE) for photons that describes Compton scattering.

### A.1. Radiative transfer equation

A description of interactions between photons and electrons via Compton scattering accounting for the induced scattering and electron degeneracy can be provided by the explicitly covariant RKE for photons (Buchler & Yueh 1976; de Groot et al. 1980; Nagirner & Poutanen 1993, 1994)

$$\begin{aligned} \underline{x} \cdot \underline{\nabla} n(\underline{x}) = & \frac{r_e^2}{2} \frac{2}{\lambda_c^3} \int \frac{d\mathbf{p}}{\gamma} \frac{d\mathbf{p}_1}{\gamma_1} \frac{d\mathbf{x}_1}{x_1} F \delta^4(\underline{p}_1 + \underline{x}_1 - \underline{p} - \underline{x}) \\ & \times \{n(\mathbf{x}_1)[1 + n(\mathbf{x})]\tilde{n}_e(\mathbf{p}_1)[1 - \tilde{n}_e(\mathbf{p})] \\ & - n(\mathbf{x})[1 + n(\mathbf{x}_1)]\tilde{n}_e(\mathbf{p})[1 - \tilde{n}_e(\mathbf{p}_1)]\}, \end{aligned} \quad (\text{A.1})$$

where  $\underline{\nabla} = \{\partial/c\partial t, \nabla\}$  is the four-gradient,  $r_e$  is the classical electron radius,  $\lambda_c = h/m_e c$  is the Compton wavelength,  $F$  is the Klein–Nishina reaction rate (Berestetskii et al. 1982)

$$F = \left(\frac{1}{\xi} - \frac{1}{\xi_1}\right)^2 + 2 \left(\frac{1}{\xi} - \frac{1}{\xi_1}\right) + \frac{\xi}{\xi_1} + \frac{\xi_1}{\xi}, \quad (\text{A.2})$$

and

$$\xi = \underline{p}_1 \cdot \underline{x}_1 = \underline{p} \cdot \underline{x}, \quad \xi_1 = \underline{p}_1 \cdot \underline{x} = \underline{p} \cdot \underline{x}_1 \quad (\text{A.3})$$

are the four-products of the corresponding momenta (second equalities in Equations (A.3) arising from the four-momentum conservation law represented by the delta-function in Eq. (A.1)). Here we define the dimensionless photon four-momentum as  $\underline{x} = \{x, \boldsymbol{\omega}\} = x\{1, \boldsymbol{\omega}\}$ , where  $\boldsymbol{\omega}$  is the unit vector in the photon propagation direction and  $x \equiv hv/m_e c^2$ . The photon distribution is described by either the occupation number  $n$  or the specific intensity (per dimensionless energy interval)  $I(\mathbf{x}) = x^3 n(\mathbf{x})/C$ , where the constant  $C$  is given by Eq. (13). The dimensionless electron four-momentum is  $\underline{p} = \{\gamma, \mathbf{p}\} = \{\gamma, p\boldsymbol{\Omega}\} = \gamma\{1, \beta\boldsymbol{\Omega}\}$ , where  $\boldsymbol{\Omega}$  is the unit vector along the electron momentum,  $\gamma$  and  $p = \sqrt{\gamma^2 - 1}$  are the electron Lorentz factor and its momentum in units of  $m_e c$ , and  $\beta$  is the velocity in units of  $c$ . The electron distribution is described by the occupation number  $\tilde{n}_e$ . For the isotropic electron distribution, we use the electron distribution function  $f_e(p) = 2\tilde{n}_e(\mathbf{p})/\lambda_c^3 N_e$ , normalized to unity

$$4\pi \int_0^\infty f_e(p) p^2 dp = 1. \quad (\text{A.4})$$

In the following, we consider a steady state and ignore electron degeneracy, because in the upper atmosphere layers, where the radiation spectrum is formed, electrons are non-degenerate. We define the RF as

$$R(\mathbf{x}_1 \rightarrow \mathbf{x}) = \frac{3}{16\pi} \int \frac{d\mathbf{p}}{\gamma} \frac{d\mathbf{p}_1}{\gamma_1} f_e(p_1) F \delta^4(\underline{p}_1 + \underline{x}_1 - \underline{p} - \underline{x}). \quad (\text{A.5})$$

For the relativistic Maxwellian distribution of temperature  $\Theta = kT_e/m_e c^2$  (Jüttner 1911; Synge 1957),

$$f_e(p) = \frac{1}{4\pi \Theta K_2(1/\Theta)} \exp(-\gamma/\Theta) \quad (\text{A.6})$$

(where  $K_2$  is the modified Bessel function), the RF satisfies the symmetry property

$$R(\mathbf{x} \rightarrow \mathbf{x}_1) e^{-x/\Theta} = R(\mathbf{x}_1 \rightarrow \mathbf{x}) e^{-x_1/\Theta}, \quad (\text{A.7})$$

which follows from its definition in Eq. (A.5) and the energy conservation  $\gamma_1 = \gamma + x - x_1$ , or from the detailed balance condition (see eq. 8.2 in Pomraning 1973). Using this result it is easy to show that the Bose-Einstein distribution  $n(x) = 1/(\exp[(x - \mu)/\Theta] - 1)$  with any chemical potential is a solution of the RKE (A.1).

In the absence of strong magnetic field, the medium is isotropic, therefore the RF depends only on the photon energies and the scattering angle (where  $\eta$  is its cosine), i.e. we can write  $R(\mathbf{x}_1 \rightarrow \mathbf{x}) = R(x, x_1, \eta)$ . The kinetic equation (A.1) can then be recast in a standard form of the radiative transfer equation

$$\begin{aligned} \frac{\boldsymbol{\omega} \cdot \nabla n(\mathbf{x})}{\sigma_T N_e} = & -n(\mathbf{x}) \frac{1}{x} \int_0^\infty x_1 dx_1 \int d^2 \omega_1 R(x_1, x, \eta) [1 + n(\mathbf{x}_1)] \\ & + [1 + n(\mathbf{x})] \frac{1}{x} \int_0^\infty x_1 dx_1 \int d^2 \omega_1 R(x, x_1, \eta) n(\mathbf{x}_1). \end{aligned} \quad (\text{A.8})$$

For the plane-parallel atmosphere, this reduces to

$$\begin{aligned} \mu \frac{dn(x, \mu)}{d\tau_T} = & n(x, \mu) \frac{1}{x} \int_0^\infty x_1 dx_1 \int_{-1}^1 d\mu_1 R(x_1, \mu_1; x, \mu) [1 + n(x_1, \mu_1)] \\ & - [1 + n(x, \mu)] \frac{1}{x} \int_0^\infty x_1 dx_1 \int_{-1}^1 d\mu_1 R(x, \mu; x_1, \mu_1) n(x_1, \mu_1), \end{aligned} \quad (\text{A.9})$$

where  $d\tau_T = -\sigma_T N_e ds = \kappa_e dm$ ,  $\mu$  and  $\mu_1$  are the cosines of the angle relative to the normal,  $\eta = \mu\mu_1 + \sqrt{1 - \mu^2} \sqrt{1 - \mu_1^2} \cos \varphi$  and

$$R(x, \mu; x_1, \mu_1) = \int_0^{2\pi} R(x, x_1, \eta) d\varphi \quad (\text{A.10})$$

is the azimuth-integrated RF. Rewriting Eq. (A.9) in terms of the intensity  $I(x, \mu)$ , we get the radiative transfer equation (10) that accounts for electron scattering with the scattering opacity and the source function given by Eqs. (12) and (14), respectively.

## A.2. Redistribution functions

The expression (A.5) for the RF can be simplified by taking the integral over  $\mathbf{p}$  with the help of the three-dimensional delta-function and using the identity  $\delta(\gamma_1 + x_1 - \gamma - x) = \gamma \delta(\underline{x}_1 \cdot \underline{p}_1 - \underline{x} \cdot (\underline{p}_1 + \underline{x}_1))$

$$R(x, x_1, \eta) = \frac{3}{16\pi} \int \frac{d\mathbf{p}}{\gamma} f_e(p) F \delta(\Gamma), \quad (\text{A.11})$$

where we have dropped the subscript 1 from the electron quantities and

$$\Gamma = \gamma(x_1 - x) - p(x_1 \boldsymbol{\omega}_1 - x \boldsymbol{\omega}) \cdot \boldsymbol{\Omega} - q, \quad (\text{A.12})$$

$$q = \mathbf{x} \cdot \mathbf{x}_1 = x x_1 (1 - \eta). \quad (\text{A.13})$$

To integrate over angles in Eq. (A.11), we follow the recipe proposed by Aharonian & Atoyan (1981) (see also Prasad et al.

1986; Poutanen & Vurm 2010), choosing the polar axis along the direction of the transferred momentum

$$\mathbf{n} \equiv (x_1 \boldsymbol{\omega}_1 - x \boldsymbol{\omega}) / Q, \quad (\text{A.14})$$

where

$$Q^2 = (x_1 \boldsymbol{\omega}_1 - x \boldsymbol{\omega})^2 = (x - x_1)^2 + 2q. \quad (\text{A.15})$$

Thus, the integration variables become  $\cos \alpha = \mathbf{n} \cdot \boldsymbol{\Omega}$  and the azimuth  $\Phi$ . The RF (A.11) can then be written as

$$R(x, x_1, \eta) = \frac{3}{16\pi} \int_1^\infty f_e(p) p d\gamma \int_0^{2\pi} d\Phi \int_{-1}^1 \delta(\Gamma) F d \cos \alpha, \quad (\text{A.16})$$

where now

$$\Gamma = \gamma(x_1 - x) - q - pQ \cos \alpha. \quad (\text{A.17})$$

Integrating over  $\cos \alpha$  using the delta-function, we get

$$R(x, x_1, \eta) = \frac{3}{8} \int_{\gamma_*}^\infty f_e(p) R(x, x_1, \eta, \gamma) d\gamma, \quad (\text{A.18})$$

where the integration over the electron distribution can be done numerically. Here we introduce the RF for monoenergetic electrons

$$R(x, x_1, \eta, \gamma) = \frac{1}{Q} \frac{1}{2\pi} \int_0^{2\pi} F d\Phi. \quad (\text{A.19})$$

We need to substitute

$$\cos \alpha = \frac{\gamma(x_1 - x) - q}{pQ} \quad (\text{A.20})$$

into the expression for  $F$ . The condition  $|\cos \alpha| \leq 1$  provides the constraint

$$\gamma \geq \gamma_*(x, x_1, \eta) = (x - x_1 + Q \sqrt{1 + 2/q})/2. \quad (\text{A.21})$$

Integrating over azimuth  $\Phi$  in Eq. (A.19) gives the exact analytical expression for the RF that is valid for any photon and electron energy (Aharonian & Atoyan 1981; Nagirner & Poutanen 1994; Poutanen & Vurm 2010), which we use in our calculations

$$R(x, x_1, \eta, \gamma) = \frac{2}{Q} + \frac{q^2 - 2q - 2}{q^2} \left( \frac{1}{a_-} - \frac{1}{a_+} \right) + \frac{1}{q^2} \left( \frac{d_-}{a_-^2} + \frac{d_+}{a_+^2} \right), \quad (\text{A.22})$$

where

$$\begin{aligned} a_-^2 &= (\gamma - x)^2 + \frac{1 + \eta}{1 - \eta}, & a_+^2 &= (\gamma + x_1)^2 + \frac{1 + \eta}{1 - \eta}, \\ d_\pm &= (a_\pm^2 - a_\mp^2 \pm Q^2)/2. \end{aligned} \quad (\text{A.23})$$

We note that the RF (A.19) satisfies the detailed balance condition (Nagirner & Poutanen 1994)

$$R(x_1, x, \eta, \gamma) = R(x, x_1, \eta, \gamma + x - x_1). \quad (\text{A.24})$$

The RF (A.11) is related to the scattering kernel (8.13) of Pomraning (1973) as  $R(x, x_1, \eta) = \sigma_s(x_1 \rightarrow x, \eta) x_1/x$ . The form given by Eq. (A.16) is equivalent to eq. (A4) of Buchler & Yueh (1976). The derived RF for monoenergetic electrons (A.22) is equivalent to eq. (A5) of Buchler & Yueh (1976) and eq. (14) of Aharonian & Atoyan (1981).

A very simple approximate expression for the RF can be obtained by assuming that the scattering in the electron rest frame proceeds in the Thomson regime (i.e. coherent) and is

isotropic. This is equivalent to substituting  $F$  by  $4/3$  in Eq. (A.19). We then get (Arutyunyan & Nikogosyan 1980; Poutanen 1994; Poutanen & Svensson 1996)

$$R(x, x_1, \eta, \gamma) = \frac{4}{3Q}. \quad (\text{A.25})$$

Integrating it over the Maxwellian distribution (A.6) gives

$$R(x, x_1, \eta) = \frac{1}{8\pi Q} \frac{e^{-\gamma_*/\Theta}}{K_2(1/\Theta)}. \quad (\text{A.26})$$

This approximate RF is also used in the calculations. We note that this RF also satisfies the detailed balance condition (A.7).

## Appendix B: Method for solving the radiation transfer equation

The formal solution of the radiative transfer equation gives a relation between the outward  $I^+(x, \mu)$  and the inward  $I^-(x, \mu) = I(x, -\mu)$  intensities at some depth point  $i$  (on the optical depth grid  $\tau_i^\pm$ ,  $i = 1, \dots, N$ ) with the adjacent intensities

$$I_i^+(x, \mu) = I_{i+1}^+(x, \mu) \exp[-(\tau_{i+1}^+ - \tau_i^+)/\mu] + \int_{\tau_i^+}^{\tau_{i+1}^+} S^+(t, x, \mu) \exp[-(t - \tau_i^+)/\mu] dt/\mu, \quad (\text{B.1})$$

$$I_i^-(x, \mu) = I_{i-1}^-(x, \mu) \exp[-(\tau_i^- - \tau_{i-1}^-)/|\mu|] + \int_{\tau_{i-1}^-}^{\tau_i^-} S^-(t, x, \mu) \exp[-(\tau_i^- - t)/|\mu|] dt/|\mu|. \quad (\text{B.2})$$

The integrals can be replaced by the sums using the parabolic approximation

$$I_i^+(x, \mu) = I_{i+1}^+(x, \mu) \exp(-\Delta\tau_{i+1}^+) + \alpha_i^+ S_{i-1}^+(x, \mu) + \beta_i^+ S_i^+(x, \mu) + \gamma_i^+ S_{i+1}^+(x, \mu), \quad (\text{B.3})$$

$$I_i^-(x, \mu) = I_{i-1}^-(x, \mu) \exp(-\Delta\tau_i^-) + \alpha_i^- S_{i-1}^-(x, \mu) + \beta_i^- S_i^-(x, \mu) + \gamma_i^- S_{i+1}^-(x, \mu), \quad (\text{B.4})$$

where

$$\begin{aligned} \Delta\tau_i^\pm &= (\tau_i^\pm - \tau_{i-1}^\pm)/|\mu|, \\ \alpha_i^- &= e_{0,i}^- + \frac{e_{2,i}^- - (\Delta\tau_{i+1}^- + 2\Delta\tau_i^-) e_{1,i}^-}{\Delta\tau_i^- (\Delta\tau_{i+1}^- + \Delta\tau_i^-)}, \\ \beta_i^- &= [(\Delta\tau_i^- + \Delta\tau_{i+1}^-) e_{1,i}^- - e_{2,i}^-] / (\Delta\tau_i^- \Delta\tau_{i+1}^-), \\ \gamma_i^- &= (e_{2,i}^- - \Delta\tau_i^- e_{1,i}^-) / [\Delta\tau_{i+1}^- (\Delta\tau_{i+1}^- + \Delta\tau_i^-)], \\ \alpha_i^+ &= (e_{2,i+1}^+ - \Delta\tau_{i+1}^+ e_{1,i+1}^+) / (\Delta\tau_i^+ [\Delta\tau_{i+1}^+ + \Delta\tau_i^+]), \\ \beta_i^+ &= [(\Delta\tau_i^+ + \Delta\tau_{i+1}^+) e_{1,i+1}^+ - e_{2,i+1}^+] / (\Delta\tau_i^+ \Delta\tau_{i+1}^+), \\ \gamma_i^+ &= e_{0,i+1}^+ + \frac{e_{2,i+1}^+ - (\Delta\tau_{i+1}^+ + 2\Delta\tau_i^+) e_{1,i+1}^+}{\Delta\tau_{i+1}^+ (\Delta\tau_{i+1}^+ + \Delta\tau_i^+)}, \end{aligned} \quad (\text{B.5})$$

and

$$\begin{aligned} e_{0,i}^\pm &= 1 - \exp(-\Delta\tau_i^\pm), \\ e_{1,i}^\pm &= \Delta\tau_i^\pm - e_{0,i}^\pm, \\ e_{2,i}^\pm &= (\Delta\tau_i^\pm)^2 - 2e_{1,i}^\pm. \end{aligned} \quad (\text{B.6})$$

At the first depth point, the coefficients are

$$\alpha_1^+ = 0, \quad \beta_1^+ = e_{1,2}^+ / \Delta\tau_2^+, \quad \gamma_1^+ = e_{0,2}^+ - \beta_1^+, \quad (\text{B.7})$$

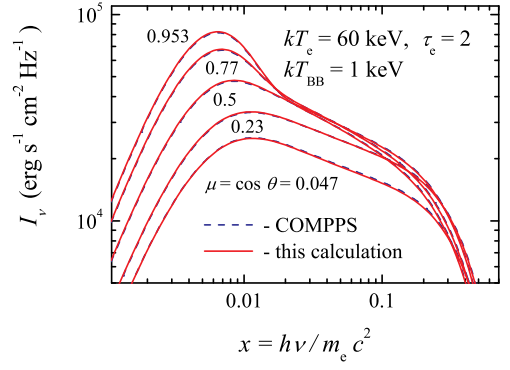


**Fig. B.1.** Comparison of the emergent spectra from a hot electron slab back-irradiated by a blackbody computed using the COMPPS code and the code presented here.

and at the last point they are

$$\alpha_N^- = e_{0,N}^- - \beta_N^-, \quad \beta_N^- = e_{1,N}^- / \Delta\tau_N^-, \quad \gamma_N^- = 0. \quad (\text{B.8})$$

We note that the inward and the outward opacities along the same ray are different (see Eq. (12)).

The formal solution for a given source function starts for the inward intensities from the outer boundary condition (the lack of incoming radiation at the surface)

$$I_1^-(x, \mu) = \beta_1^- S_1^-(x, \mu) + \gamma_1^- S_2^-(x, \mu) \quad (\text{B.9})$$

up to the last depth point  $N$ . The intensities at the innermost depth point are found using the inner boundary condition, which is taken from the diffusion approximation

$$I_N^+(x, \mu) = I_N^-(x, \mu) + 2 \frac{B_{x,N} - B_{x,N-1}}{\Delta\tau_N}. \quad (\text{B.10})$$

The full solution is found iteratively using an accelerated  $\Lambda$ -iteration. At the first iteration, the thermal part of the source function is taken. For the subsequent iteration  $n$ , the intensities obtained from the previous iteration  $n - 1$  are used to compute the current source functions  $S_i^{\pm,n}$ . Iterations are continued until the relative change becomes smaller than the predetermined accuracy

$$\max \left[ \frac{J_i^n(x)}{J_i^{n-1}(x)} - 1 \right] < 10^{-4}, \quad (\text{B.11})$$

where  $J_i(x)$  are the mean intensities. This solution method of the radiation transfer equation was tested for a rather optically thin (Thomson optical depth  $\tau_T = 2$ ) and hot ( $kT_e = 60$  keV) electron slab back-illuminated by soft blackbody photons of  $kT_{BB} = 1$  keV. The solution for the emergent intensities obtained at five angles using our method were compared with the solution obtained with the Comptonization code COMPPS (Poutanen & Svensson 1996, see Fig. B.1).

In the optically thick case ( $\tau_T \gg 1$ ), which is typical of NS atmospheres, the convergence of the solution can be accelerated using the following procedure. The difference between the formal solution obtained in the current iteration  $I_i^{\pm,n,FS}$  and the solution at iteration  $n - 1$  is increased by some factor

$$I_i^{\pm,n}(x, \mu) - I_i^{\pm,n-1}(x, \mu) = \frac{I_i^{\pm,n,FS}(x, \mu) - I_i^{\pm,n-1}(x, \mu)}{1 - \epsilon_i^{\pm,n}(x, \mu) \Lambda_{i,i}^*(x, \mu)}, \quad (\text{B.12})$$

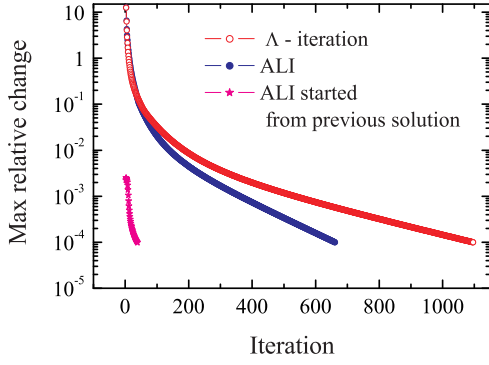


**Fig. B.2.** The maximum relative change in the solution of the radiation transfer equation at the final temperature correction computed by different versions of the accelerated  $\Lambda$ -iteration.

where

$$\varepsilon_i^{\pm,n}(x, \mu) = \frac{\sigma_i^{\pm,n}(x, \mu)}{\sigma_i^{\pm,n}(x, \mu) + k_i(x)}, \quad (\text{B.13})$$

and  $\Lambda_{i,i}^*(x, \mu)$  is the diagonal term of the approximate  $\Lambda$ -operator

$$\Lambda_{i,i}^*(x, \mu) = \frac{1}{4}[\beta_i^+(x, \mu) + \beta_i^-(x, \mu)] \times x^2 \int_0^\infty \frac{dx_1}{x_1^2} \int_{-1}^1 d\mu_1 R(x, \mu; x_1, \mu_1). \quad (\text{B.14})$$

The acceleration is not high (about 30 – 40 %) and the number of necessary iterations is still large (see Fig. B.2). However, in the process of the model atmosphere computation it is possible to use the source function from the previous temperature iteration as the starting approximation for the current source function (see details in Section 2). In this case, the acceleration depends on the value of the temperature corrections  $\Delta T_i$ . At the first few temperature iterations, when  $\Delta T_i$  are large, the acceleration is insignificant, but at later iterations, when  $\Delta T_i$  are relatively small, the accelerated  $\Lambda$ -iterations converge very quickly (Fig. B.2).

### Appendix C: Comparison with Madej's code

The only other attempt to compute NS atmospheres using an integral approach to Compton scattering going beyond the Kompaneets approximation was that of J. Madej and collaborators (Madej 1991; Madej et al. 2004; Majczyna et al. 2005). They used an angle-averaged RF for Compton scattering derived by Guilbert (1981). It is important to compare our results with those obtained by Madej's code for the same input parameters. We selected our fiducial model as a testbed and computed two models. In the first, we approximated electron scattering by coherent Thomson scattering. In the second, the exact fully relativistic RF for Compton scattering was used. Calculations for identical parameters were performed with Madej's code (J. Madej and A. Różańska, private communication). A comparison between the results is shown in Fig. C.1.

We see that the Thomson scattering models are very close to each other, in terms of both the spectra and the temperature structures (Fig. C.1, *left panels*). However, the models with Compton scattering differ substantially (Fig. C.1, *right panels*). Temperatures in the upper layers with column densities less than  $10^3 \text{ g cm}^{-2}$  are lower in our model by up to 5–15%, and our

spectrum (solid curve) is much more peaked and softer than that computed by Madej's code (dashed curve). We also note that our spectrum is very close to the diluted blackbody spectra, which cannot be said about Madej's spectrum.

We can suggest two hypotheses to explain the discrepancies. First, there is a difference in the RF used by the two codes. We employed the exact relativistic RF (see Appendix A.2), which had been extensively studied and tested against Monte-Carlo simulations (Stern et al. 1995; Zdziarski et al. 2000). Madej and collaborators (Madej 1991; Madej et al. 2004; Majczyna et al. 2005) used the (angle-averaged) RF derived by Guilbert (1981) (see his Eqs. (8) and (10)), which differs from the correct expression (A.19) by an additional factor  $[1 - (\beta \cdot \mathbf{n})(\mathbf{n} \cdot \boldsymbol{\omega}_1)] / (1 - \beta \cdot \boldsymbol{\omega}_1)$ , which appeared from an error in the Jacobian. Guilbert's RF also does not satisfy the detailed balance condition (A.24) and therefore the RF integrated over the electron distribution does not satisfy the condition (A.7) either. Because the energy transfer by Compton scattering scales as  $\beta^2$ , the error on the order of  $\beta$  obviously invalidates all the results obtained with this RF.

Second, some of the discrepancies could be connected to a difference in the computation of the radiation transfer and the atmosphere modeling. We illustrate this in Fig. C.1 (*top right panel*). Using our radiation transfer code, we computed the spectrum using the temperature structure from Madej's calculations. When calculations proceeded until the accuracy of  $10^{-4}$  was reached (dotted curve), the spectrum was much above our benchmark spectrum, i.e. it had a much higher effective (and color) temperature. If calculations were stopped at a lower accuracy of  $10^{-2}$  (dash-dotted curve), the spectrum was found to be similar to Madej's spectrum. This suggests that the radiation transfer iterations with Madej's code did not sufficiently converge.

Madej et al. use the partial linearization method described in Mihalas (1978, p. 179) and modified to include Compton scattering. Their radiation transfer equation is rewritten to include the linearized part of the radiative equilibrium equation. The solution of this generalized radiation transfer equation satisfies simultaneously the radiative equilibrium to the first order. Using the computed radiation field, the temperature correction for the current temperature structure of the atmosphere is found. This procedure is iterated until some convergence criterion is satisfied, for example, the emergent bolometric flux is accurate to within 0.1 %. In this method, the accuracy of the current solution of the radiation transfer equation is on the order  $\Delta T/T$ , which is about  $10^{-2}$ – $10^{-3}$  at the last iteration. We have shown above that this internal accuracy is insufficient to obtain the exact solution of the radiation transfer equation when Compton scattering is taken into account. We note that using this method is not possible to solve the radiation transfer equation for a given atmosphere model or, for example, for a homogeneous isothermal slab. This means that it cannot be checked independently of the atmosphere modeling.

### Appendix D: Atmosphere model spectra and color-corrections

Table D.1 gives the color-correction and dilution factors from the blackbody fits to 484 atmosphere model spectra (fluxes), which in their turn are given in Table D.2. Table D.3 contains the emergent specific intensities at three angles. Tables D.1, D.2 and D.3 are only available in electronic form at the CDS via anonymous ftp to cdsarc.u-strasbg.fr (130.79.128.5) or via <http://cdsweb.u-strasbg.fr/cgi-bin/qcat?J/A+A/>.

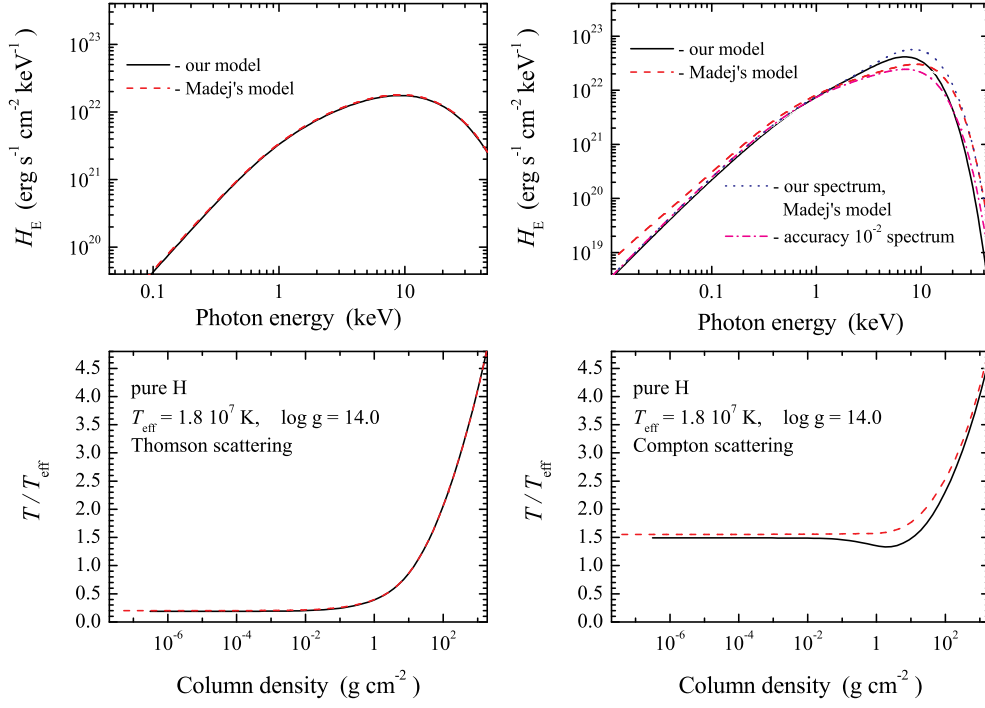


**Fig. C.1.** *Left panels:* Comparison of emergent spectra and temperature structures of the models computed by our code (solid curves) and Madej's code (dashed curves), when electron scattering is approximated by coherent Thomson scattering. *Right panels:* Same as left, but when the exact RF was used to compute Compton scattering. The spectrum computed by us using the Madej's temperature structure is shown by the dotted curve and the spectrum computed with a relative accuracy of  $10^{-2}$  is presented by dash-dots.